Raman spectroscopy of femtosecond multipulse irradiation of vitreous silica: Experiment and simulation

N. S. Shcheblanov,[1,2] M. E. Povarnitsyn,[3] K. N. Mishchik,[4,5] and A. Tanguy[6]

[1]*Centre de Physique Théorique, CNRS, École Polytechnique, Université Paris-Saclay, F-91128 Palaiseau, France*

[2]*Laboratoire des Solides Irradiés CEA-CNRS, École Polytechnique, Université Paris-Saclay, F-91128 Palaiseau, France*

[3]*Joint Institute for High Temperatures, RAS, 13 Bld. 2 Izhorskaya Str., 125412 Moscow, Russia*

[4]*Amplitude Systèmes, 11 Avenue de Canteranne, Cité de la Photonique, F-33600 Pessac, France*

[5]*Laboratoire Hubert Curien, UMR5516 CNRS, Université de Lyon, Université Jean Monnet, F-42000 Saint-Etienne, France*

[6]*Université de Lyon, LaMCoS, INSA-Lyon, CNRS UMR5259, F-69621 Villeurbanne Cedex, France*

(Received 16 October 2017; published 13 February 2018)

We report an experimental and numerical study of femtosecond multipulse laser-induced densification in vitreous silica (v-SiO_2) and its signature in Raman spectra. We compare the experimental findings to the recently developed molecular dynamics (MD) approach accounting for bond breaking due to laser irradiation, together with a dynamical matrix approach and bond polarizability model based on first-principles calculations for the estimation of Raman spectra. We observe two stages of the laser-induced densification and Raman spectrum evolution: growth during several hundreds of pulses followed by further saturation. At the medium range, the network connectivity change in v-SiO_2 is expressed in reduction of the major ring fractions leading to more compacted structure. With the help of the Sen and Thorpe model, we also study the short-range order transformation and derive the interbonding Si–O–Si angle change from the Raman measurements. Experimental findings are in excellent agreement with our MD simulations and hence support a bond-breaking mechanism of laser-induced densification. Thus, our modeling explains well the laser-induced changes both in the short-range order caused by the appearance of Si coordination defects and medium-range order connected to evolution of the ring distribution. Finally, our findings disclose similarities between sheared, permanently densified, and laser-induced glass and suggest interesting future experiments in order to clarify the impact of the thermomechanical history on glasses under shear, cold and hot compression, and laser-induced densification.

DOI: 10.1103/PhysRevB.97.054106

I. INTRODUCTION

Comprehension of the processes of laser-induced modification in vitreous silica (v-SiO_2) and their control remains an important research issue. This concerns the accurate design of the optical properties via local laser-induced refractive index changes (RIC), serving in the fabrication of embedded optical components in fibers and bulk materials [1–3]. The densification of v-SiO_2 due to laser irradiation seems reasonable to cause a uniform RIC [4,5]. The supporting evidence of this mechanism was provided by micro-Raman spectroscopy for both single- [6,7] and multipulse [8–14] experiments. In these experiments, the analyses were mainly focused on the strongest band ($\sim$437 cm^{-1}) and defect lines D_1 ($\sim$495 cm^{-1}) and D_2 ($\sim$605 cm^{-1}), usually related to four-membered and three-membered rings (or four- and threefold), respectively. Analysis of network connectivity in terms of rings is still a topic of discussion [15–18]. In the above mentioned experiments, it was shown an increase of the intensity of the D_2 band, together with a stagnation of the D_1 band (in opposition with cold compressed glasses [19,20]. In Ref. [5], we treated the hypothesis of the bond-breaking mechanism leading to v-SiO_2 densification under laser irradiation. We addressed the medium-range order and explained in detail the behavior of defect line D_2, relying on the connection between population of the threefold rings and D_2 lines. However, all these previous Raman measurements indicating material sensitivity to laser irradiation were not compared to numerical Raman results [9,11,14,21], and no Raman data are available for successive laser-induced experiments in the high-frequency range ($\sim$900–1300 cm^{-1}).

In parallel, intensive studies of v-SiO_2 glass are continuing, aimed at studying the role of thermomechanical history in densification [20,22,23] and plastic shear [24] where, in particular, a specific sensitivity of Raman spectra in the high-frequency range is observed. In order to infer structural information from Raman spectra in silica glasses, the Sen and Thorpe (ST) analysis [25] relating the position of the characteristic bands to interbonding angle is usually applied [26,27].

Here, we present a systematic analysis of the effect of a multipulse femtosecond laser on vibrational properties, Raman spectra, and medium- and short-range structure with the help of numerical calculations compared to experimental measurements of Raman spectra.

II. METHODS

A. Experiment

The sketch in Fig. 1 shows the multiscale nature of the writing processes involved in the consideration. Femtosecond laser pulses are produced by a regeneratively amplified Ti:sapphire laser system at 800 nm with a nominal pulse duration of

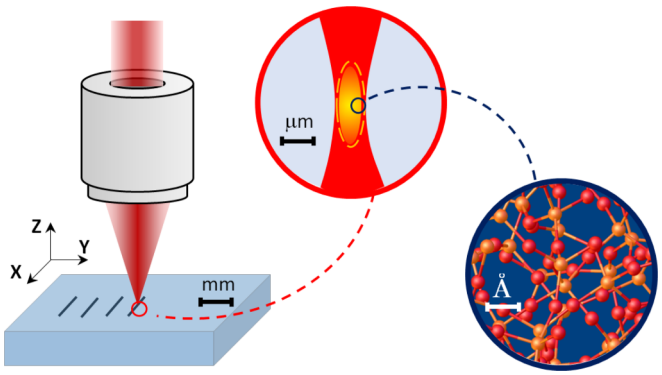

FIG. 1. Schematic representation of the femtosecond laser writing. At macroscale, the laser beam is focused inside the bulk of v-SiO_2 via the objective. At microscale, photoionization conditions are realized in the focal area. At nanoscale, the structure of v-SiO_2 is composed of network-forming species Si (orange) and O (red) undergoing bond breaking due to photoionization.

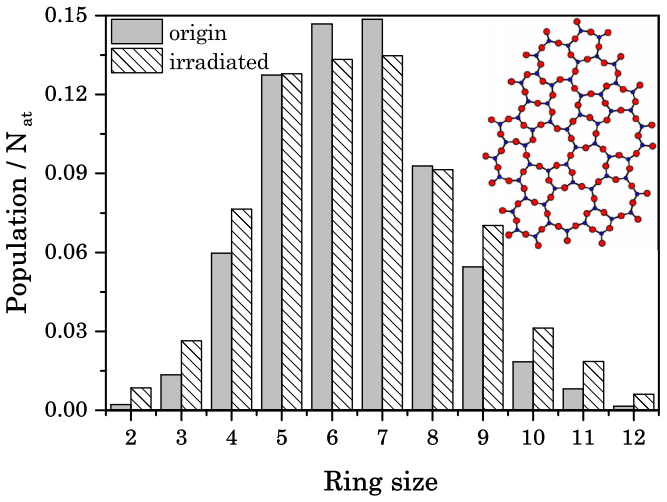

FIG. 2. Evolution in the distribution of rings in v-SiO_2. Gray shaded distribution corresponds to origin samples. Patterned distribution corresponds to samples irradiated by 800 pulses. The results of modeling are obtained by averaging over 10 samples. Number of atoms: $N_{at} = 8232$. Inset: Two-dimensional schematic diagram of the v-SiO_2 network with added colors [29].

$\tau_p = 130$ fs (FWHM) and an energy 1 μJ. The long working distance, a 20× microscope objective (Mitutoyo MPlan, NA = 0.42, $f = 10$ mm), is employed to focus the ultrashort laser pulses into the bulk of silica [10]. A laser beam diameter is less than the objective pupil ($d = 5$ mm at the level $1/e^2$); therefore the nominal value of NA is corrected to $NA_{eff} = 0.3$. Polished high-purity synthetic fused silica (Corning 7980-5F, 800–1000 ppm concentration of OH impurities) samples are mounted on a XYZ motion stage. By varying the speed of the sample translation perpendicular to the laser propagation axis, we control the number of pulses in the writing of long waveguiding structures. The modifications are produced at a 10-kHz laser repetition rate, when the material is thermally relaxed before the new pulse arrival. This is in agreement with other reports indicating that the heat accumulation effect in silica plays an important role only in the megahertz regime of irradiation [28].

Laser modification results in uniform positive refractive index changes of exposed volume (type-I structures [30]), which is confirmed by the waveguiding properties of the written structures and additionally verified using phase contrast microscopy. The Raman spectra of the irradiated samples are recorded with a Horiba Jobin Yvon confocal microspectrometer in a backscattering configuration. The laser excitation is performed using a HeCd source at 442-nm wavelength. The arrangement allows for a spatial resolution better than 1 μm and a spectral resolution of 3 cm^{-1}.

B. MD simulation

In our study, the v-SiO_2 model is prepared following the work of Ref. [31]. A system of 8232 atoms (size ∼5 nm) is obtained within molecular dynamics (MD) simulation (via LAMMPS [32]) using a melt-quench procedure [33], and the quenching rate is 5.2×10^{13} K s^{-1}. The equilibration of the liquid, quench, and relaxation of the glass is performed classically using the van Beest, Kramer, and van Santen (BKS) potential [34] modified by Carré *et al.* [35] (see Appendix A). The BKS potential was thoroughly examined and it was found that it reproduces many structural and dynamical properties of real silica very well [36,37]. Among them are the static structure factor, the glass transition temperature, and the activation energies of the viscosity and the diffusion constants. By evolving the BKS samples during 10,20 . . . 100 ns at liquid stage, we obtain ten v-SiO_2 models at density of 2.2 g cm^{-3}.

In order to consider the interaction of subpicosecond laser pulses with v-SiO_2, we introduced a bond-breaking mechanism into the MD scheme [5]. The whole simulation cycle of a laser pulse interaction with an MD glass model is as follows. The simulation starts from an instantaneous generation of broken bonds emulating the laser pulse excitation stage. According to a given ionization degree (a percentage of ionized valence band electrons), we determine the number of broken Si-O bonds for the simulation box; then we choose randomly their positions in a space. We are of the opinion that a bond is broken due to irradiation if the corresponding Si and O atoms supported this bond do not interact with each other; however, their attached neighbors keep having common bonds. The ionization degree is 0.018%, corresponding to two broken bonds per sample (or free electron density 1.6×10^{19} cm^{-3}). At the second step, the excited electrons transfer energy to the atomic system heating the sample. The temperature saturates with time, reaching the maximum value (500 K). Therefore, we evolve our glass sample during the next 5 ps at 500 K. Subsequently, at the third step, a cooling to the room temperature, 300 K, occurs during 100 ps. Eventually, when the laser-excited electrons become trapped or relaxed (i.e., at the end of the cooling stage), we repair an interaction ability for the Si and O atoms (early constituted broken bonds) conforming to used potential. In some events (due to the bond breaking) the broken bonds return to the original ones, and in other events not. Our approach implies that the environment responds to local loss of rigidity due to the bond breaking. Note that the local evolution, induced by laser irradiation, can be more complicated than that in our simulation, and, therefore, a local rigidity of a given bond could vanish incompletely [38]. However, the final

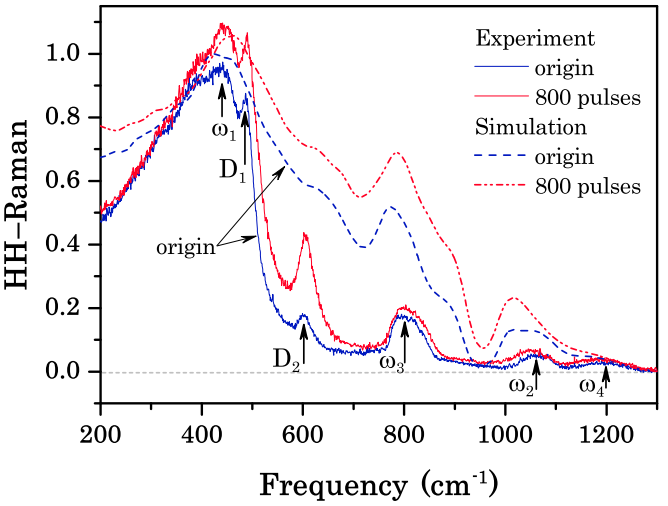

FIG. 3. HH-Raman spectra in v-SiO_2. Experimental data: origin sample–solid blue, after irradiation–solid red. The simulation results: origin–dashed blue, after irradiation–solid dash-dot red. The results of simulation are averaged over ten configurations. Reference frequencies discussed in the text are $\omega_1 = 437$ cm^{-1}, $\omega_3 = 800$ cm^{-1}, $\omega_2 = 1060$ cm^{-1}, $\omega_4 = 1200$ cm^{-1}.

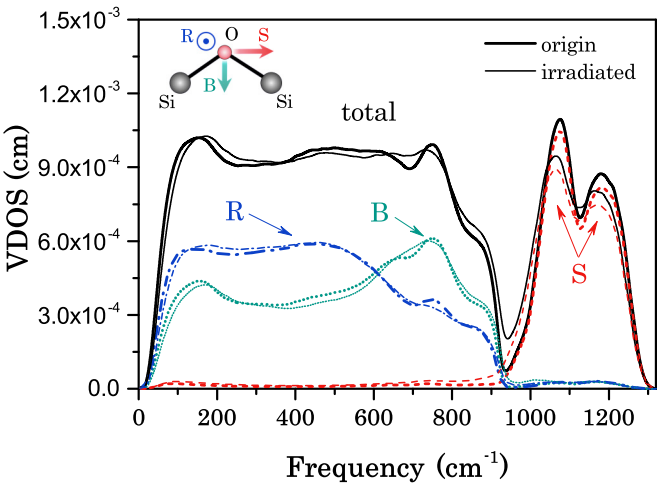

FIG. 4. The partial VDOS for the projections onto the vibrations of Si–O–Si structural units: stretching–dashed red, bending–dotted green, rocking–dash-dot blue, and total–solid black. Origin sample–thick curves, after irradiation by 800 pulses–thin curves. Inset shows the relative motion of the oxygen atoms decomposed into stretching (S), bending (B), and rocking (R) components.

local relaxation of broken bond is not able to expand the environmental network. Thus, the laser-induced densification in silica [5] is caused by many small rearrangements, leading to compaction of the sample and not local evolution (densification) in the vicinity of a certain breakage, i.e., a breakage is only a trigger for other bonds from the environmental network. Finally, an annealing at room temperature is applied. We repeat this cycle a required number of times to simulate multipulse laser irradiation (up to 1000 pulses).

C. Raman model

In our previous study we established that the laser-induced densification of v-SiO_2 is traced to medium-range changes in topology of the atomic network. These changes consist in an increase of network connectivity caused by the reduction of major ring fractions of six- and seven-membered rings to minor fractions of three- and four-membered rings [5]. In Fig. 2 we show the evolution in the distribution of rings in v-SiO_2 upon multipulse irradiation. However, it is impossible to directly extract ring statistics or local ring environments in the bulk from experimental measurements. Nonetheless, by applying the Raman spectroscopy, enabling the vibrational analysis to be performed at micrometer scale, we can infer the information at medium-range and short-range order.

Here, we briefly outline the formulation that we use for the calculation of Raman activities. We focus only on first-order processes, which involve a single phonon excitation. In the Stokes process, in which a vibrational excitation is created by an incoming photon, we express the total power cross section as (in esu units) [39]

$$\mathcal{I}^P(\omega) = \frac{2\pi\hbar}{\omega}\,\frac{g(\omega)(\omega_L-\omega)^4}{V^{-1}c^4}\sum_n \mathcal{I}_n\,\delta(\omega-\omega_n), \quad (1)$$

where the index n labeling the vibrational modes runs from 1 to $3N_{\rm at}$, $N_{\rm at}$ is the total number of atoms in the model (8232 atoms), ω_L is the frequency of the incoming photon, c is the speed of light, V is the volume of the scattering sample, $g(\omega) = n_B(\omega) + 1$, and $n_B(\omega)$ is the boson factor. In experimental setups, it is customary to record the Raman spectra in the horizontal-horizontal (HH) configuration in which the polarization of the outgoing photons is respectively parallel to the ingoing photon polarization [40]. Using the isotropy of disordered solids, we express the contribution of the nth mode $\mathcal{I}_n$ to the HH-Raman spectra as [39]

$$\mathcal{I}_n^{HH} = a_n^2 + \frac{4}{45}b_n^2, \quad (2)$$

where a_n and b_n are obtained from

$$a_n = \frac{1}{3}\sum_i^3 \mathcal{R}_{ii}^n, \quad (3)$$

$$b_n^2 = \sum_{i<j}^3 \left\{\frac{1}{2}\left(\mathcal{R}_{ii}^n - \mathcal{R}_{jj}^n\right)^2 + 3\left(\mathcal{R}_{ij}^n\right)^2\right\}. \quad (4)$$

The Raman susceptibility tensors $\mathcal{R}_{ij}^n$ are given by [39]

$$\mathcal{R}_{ij}^n = \sqrt{V}\sum_{I,k}\frac{\partial\chi_{ij}}{\partial R_{Ik}}\frac{\xi_{Ik}^n}{\sqrt{M_I}}, \quad (5)$$

where $\boldsymbol{\chi}$ is the electric polarizability tensor, the capital Latin indices run over the atoms, the lowercase Latin indices are the three Cartesian directions, $\mathbf{R}_I = (R_{I1}, R_{I2}, R_{I3})$, and M_I are the position and the atomic mass of atom I, respectively. In order to compute $\boldsymbol{\chi}$, we apply the bond polarizability model [41,42] (see Appendix B). For a model system, the vibrational frequencies ω_n^2 and their associated eigenmodes $\boldsymbol{\xi}_I^n$ are found by solving the set of linear equations

$$\sum_{Jj} D_{Ii,Jj}\xi_{Jj}^n = \omega_n^2\xi_{Ii}^n, \quad (6)$$

where **D** is the dynamical matrix, which is defined by

$$D_{Ii,Jj} = \frac{1}{\sqrt{M_I M_J}} \frac{\partial^2 E_{\text{tot}}}{\partial R_{Ii} \partial R_{Jj}} \text{ for } I \neq J, \tag{7}$$

$$D_{Ii,Ij} = -\sum_{J \neq I} \frac{1}{M_I} \frac{\partial^2 E_{\text{tot}}}{\partial R_{Ii} \partial R_{Jj}}, \tag{8}$$

where E_{tot} is the global potential energy of the system (see Appendix A).

The result of the Raman simulations of v-SiO_2 are presented in Fig. 3. One can see that the main characteristics of the experimental spectra are recovered within our semiclassical approximation. In the Raman spectrum, we can recognize well the main band (∼400–550 cm^{-1}) as well as the high-frequency bands, in particular, those located at ∼800 cm^{-1}, ∼1060 cm^{-1}, and ∼1200 cm^{-1}, that are well reproduced by our simulation.

The assignment of the vibration modes of v-SiO_2 is well documented [43–46]. Performing projectional analysis (see Appendix C), we decompose the vibrational density of states (VDOS) for relative motions of the oxygen atoms into stretching, bending, and rocking components (see Fig. 4). The VDOS reveals the pure stretching nature of the high-frequency doublet zone (∼950–1300 cm^{-1}), and the bending and rocking modes are in the range ∼0–900 cm^{-1}. In all the spectra of Figs. 3 and 4, the high-frequency part of the spectra ($\gtrsim$950 cm^{-1}) almost exclusively results from stretching vibrations. As far as the HH-Raman spectrum is concerned, Umari and Pasquarello showed that the bending motions dominate the rest of the spectrum (∼100–900 cm^{-1}), whereas the contribution of rocking vibrations is suppressed with respect to their weight in the VDOS [46].

III. RESULTS AND DISCUSSION

Comparing the experimental and modeling Raman spectra from Fig. 3, we highlight that the laser-induced changes in all bands have a similar tendency to each other. In particular, one can observe a raise and a slight shift to the right of the main band ω_1; the ω_3 band has a weaker raise and a slight shift to the right. On the contrary, we can indicate the more significant changes in the high-frequency doublet zone, a shift to the left of ω_2 and ω_4 bands. In the experimental spectrum, one can see a significant gain of defect lines D_1 and D_2, whereas our simulation suffers due to the lack of resolution in these areas. However, the D_1 and D_2 Raman defect lines are usually associated with four- and threefold rings in the structure of v-SiO_2 [16]. Since these lines provide direct information on the concentration of these rings [47], we characterize the medium-range structure (network connectivity) by analyzing the ring distribution instead of a direct Raman analysis of the defect lines. Our previous work was dedicated to this point [5], where a good agreement with experiment was obtained, which is a strong argument in favor of the proposed model; this shortcoming (lack of resolution in $D_{1,2}$ areas) does not affect the following discussions and conclusions of the present paper. It is also interesting to note that the global increase in the Raman intensity in the intermediate-frequency range, and the shift of the high-frequency bands in both Raman and VDOS (see Fig. 4) spectra share more similarities with the Raman and VDOS signatures of plastic-shear [24] and permanently densified glass [19,26,27,48].

In order to explain the changes in the Raman spectra upon multipulse laser irradiation, we exploit a simple central-force ST model to describe the dynamics of covalently bonded networks [25]. Reference [25] assumed that the vibrations of the silica network can be described using Si–O–Si units with only one force constant α defined by the Si–O bond. The following equations were proposed to describe the positions of the vibrational bands as a function of interbonding angle ϑ:

$$\omega_1^2 = \frac{\alpha}{M_{\text{O}}}(1 + \cos\vartheta), \tag{9a}$$

$$\omega_2^2 = \frac{\alpha}{M_{\text{O}}}(1 - \cos\vartheta), \tag{9b}$$

$$\omega_3^2 = \omega_1^2 + \frac{4\alpha}{3M_{\text{Si}}}, \tag{9c}$$

$$\omega_4^2 = \omega_2^2 + \frac{4\alpha}{3M_{\text{Si}}}, \tag{9d}$$

where M_{O} and M_{Si} are the masses of oxygen and silicon atoms, respectively.

To extract information about the angle change from Raman spectra applying the ST model, one needs to determine the central-force constant. By using the measured Raman frequencies ω_i (see Fig. 3) and mean Si–O–Si angle, $\vartheta = 147.7°$, taken from [49,50], the force constants α_{1-4} are calculated by Eqs. (9a)–(9d), respectively. The values of α are presented in Table I. It can be seen that $\alpha_1(\omega_1) \approx 1170$ N/m differs significantly from other values. It is known that the modes in the middle of the lower band are not so well localized in silica [43], whereas the ST model implies local vibrations. Structural disorder in silica leads to a broad Si–O–Si angle distribution (∼135°–160° [49]) and a broadening of vibrational bands. As a result, an asymmetry and a wide width of the ω_1 band (∼100–500 cm^{-1}) leads to an ambiguity in the calculation of α_1 and α_3 [see Eqs. (9a) and (9c)]. However, if we take instead of the frequency $\omega_1 = 437$ cm^{-1} (corresponding to the maximum of the band) the frequency $\omega_g \approx 340$ cm^{-1} corresponding to the center of gravity of the ω_1 band, then $\alpha_1(\omega_g) \approx 710$ N/m and $\alpha_3(\omega_g) \approx 653$ N/m. We also take into account the fact that the high-frequency doublet zone is comprised of symmetric and asymmetric stretching modes [43,44] which are quite well localized but interfere with each other. The shift of the decomposed location with respect to enveloped location (1200 cm^{-1}) for the stretching modes (ω_4) gives $\omega_4' \approx 1225$ cm^{-1} and $\alpha_4 \approx 469$ N/m. Thus, all α_{1-4} according to the ST model are in fair agreement with each other.

TABLE I. Force constants. $\bar{\alpha} = (\alpha_1 + \alpha_2 + \alpha_3 + \alpha_4)/4$, where α_{1-4} are calculated by Eqs. (9a)–(9d), respectively.

Force constant	α_1	α_2	α_3	α_4	$\bar{\alpha}$
N/m	1170.1	577.3	558.8	394.0	674.9
	$\alpha_1(\omega_g)$	α_2	$\alpha_3(\omega_g)$	$\alpha_4(\omega_4')$	$\bar{\alpha}$
N/m	710	577.3	653	469	602

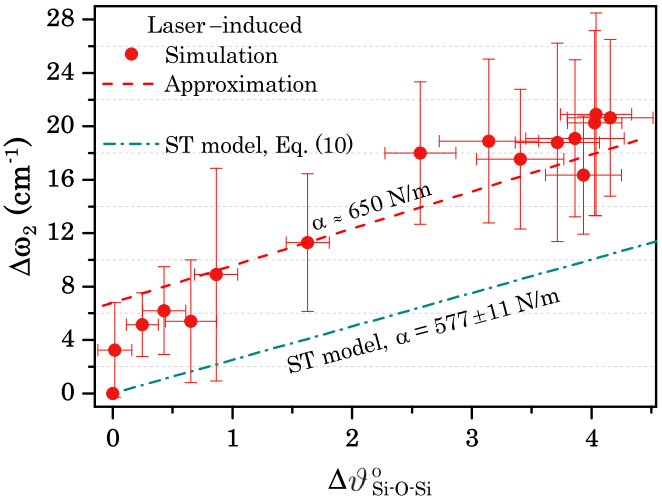

FIG. 5. Simulation of laser-induced HH-Raman ω_2 shift versus mean Si–O–Si angle change–filled red circles (half-width at half-maximum fitting). The dashed red line shows the approximation of the simulation data. The results of modeling are averaged over ten samples. The dash-dot green line shows a ω_2 shift based on the ST model [25], Eq. (10), at the following parameters: central-force constant $\alpha = 577$ N/m (calculated using measured Raman characteristic frequency ω_2, see Fig. 3) and mean Si–O–Si angle $\vartheta = 147.7 \pm 3.8^\circ$ [49].

As shown in [51], the interbonding angle change $\Delta\vartheta$ can be related to the ω_2 shift by differentiating Eq. (9b) to obtain

$$\Delta\omega_2 = \frac{\alpha}{2M_O}\frac{\sin\vartheta\,\Delta\vartheta}{\omega_2}. \tag{10}$$

Our simulation and experimental measurements provide good resolution of the Raman ω_2 band. Furthermore, we choose the ω_2 band to treat the experimental measurements because the corresponding α_2 is closer to the mean value of central-force constant $\bar{\alpha}$, see Table I.

In Fig. 5 we present the simulation results of ω_2 shift as a function of mean interbonding angle change obtained by irradiation with different numbers of pulses. The mean interbonding angle is derived from MD simulation using the coordinates of atoms. As a result, we can see that our simulations predict the linear behavior confirming the ST model, see Eq. (10). Moreover, the central-force constant values obtained from the simulation ($\alpha \approx 650$ N/m) and calculated using the measured Raman characteristic frequency ω_2 ($\alpha \approx 577$ N/m) are in good agreement. Thus, we demonstrate that the ST model is applicable to describe the Raman dynamics upon multiple laser irradiation.

The dynamics of $\Delta\omega_2$ with the pulse number is shown in Fig. 6(a). On can reveal two stages of dynamics—the growth during several hundreds of pulses followed by saturation, both in simulation and experiment. Despite averaging over ten samples, we note the sharp rise of the ω_2 shift in the very beginning and noticeable dispersion in simulation that we ascribe to the size of the models (see Sec. II B). This size effect will be reduced in our further investigations by increasing the number of atoms in the samples. We can also observe two stages, growth and saturation, in the densification dynamics, which correlates quite well with the ω_2 shift, but it is rather smooth compared to the ω_2 shift. We guess that the saturation level depends on the given ionization degree (equivalent to a certain laser intensity in experiment) and hence may be different at different degrees.

Applying the ST model to the ω_2 shift experimental findings from Fig. 6(a), we extract the corresponding angle change. One can see that the interbonding angle change follows the ω_2 shift and also reproduces the two-stage dynamics: the growth during ~600 pulses followed by saturation, see Fig. 6(b). The comparison shows an excellent agreement between experiment

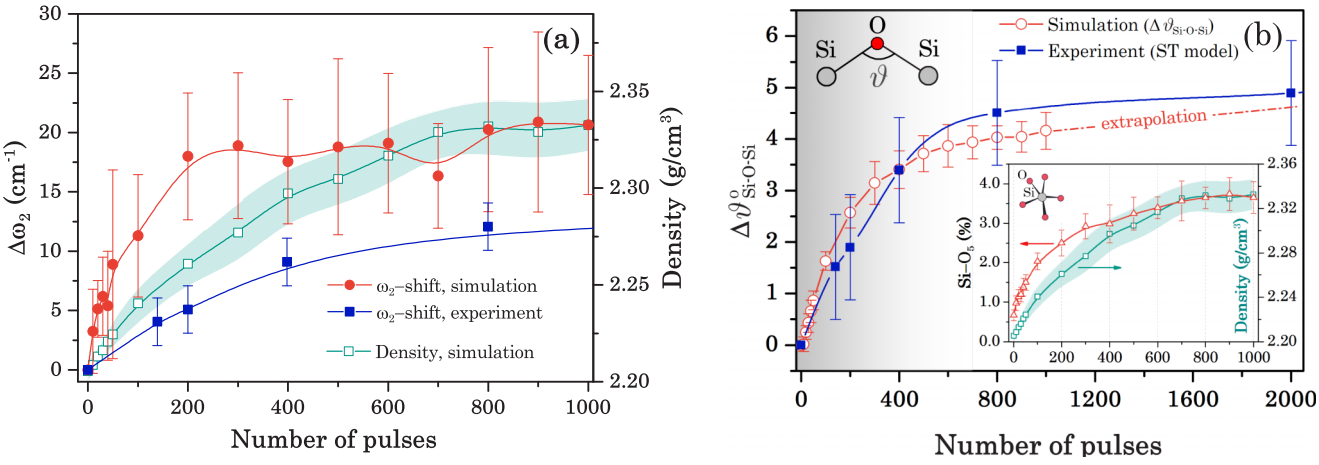

FIG. 6. (a) Absolute value $\Delta\omega_2$ of the laser-induced HH-Raman ω_2 shift as a function of pulse number: experiment–filled blue squares; simulation–filled red circles, compared to density change obtained in simulation–empty green squares with density dispersion depicted by the shaded green area. (b) Si–O–Si angle change versus pulse number. Experimental results via ST model–filled blue squares; results of simulation–empty red circles. Inset: Change of number of five-coordinated Si atoms at degree of ionization 0.018% in simulation as a function of pulse number–empty red triangles. Corresponding density–empty green squares with error bar depicted by shaded light green area. The results of modeling are averaged over ten samples. The number of pulses 140, 200, 400, and 800 in simulation exactly corresponds to that in experiment.

and MD simulation. Since we reveal the densification, we guess that laser-induced rearrangements should lead to transformations of the v-SiO_2 network both in the medium-range [5] and short-range order. The short-range structure is usually characterized by coordination number [52,53]. We found here a correlation between the growth of five-coordinated Si atoms and v-SiO_2 densification upon laser irradiation, see inset in Fig. 6(b). Similar behavior was observed in permanently densified [54,55] and high-pressure-induced [52,53,56,57] silica glass. Thus, we relate the Si–O–Si angle decline to the increase of network connectivity caused by the reduction of the major ring fractions [5] and the increase in coordination defects (five-coordinated Si atoms) due to multipulse laser irradiation.

IV. CONCLUSIONS

In summary, our systematic Raman calculation shows that upon multipulse laser irradiation the SiO_2 glass undergoes several successive transformations both in short-range and medium-range order. The changes in the Raman measurements are well described by our simulations within the numerical accuracy. This reinforces our previously developed model of bond breaking for laser irradiation [5]. In experiment and simulation, two stages of the laser-induced densification and Raman spectrum evolution are observed: growth during several hundreds of pulses followed by further saturation. At the medium range, the network connectivity is expressed in reduction of the major ring fractions, leading to more compacted structure. By using the Raman measurements and the ST model, we highlight the short-range transformation by extracting the dynamics of Si–O–Si angle change. These results are in excellent agreement with our simulation results. In addition, we show a correlation between the growth of five-coordinated Si atoms and densification due to laser irradiation. Thus, we conclude that the laser-induced densification of v-SiO_2 is related to the changes in the short-range order caused by the appearance of Si coordination defects and medium-range order connected to evolution of the ring distribution. These findings disclose similarities between laser-induced and permanently densified glasses [54,55,58]. Moreover, our preliminary analysis shows more generally that the sensitivity of the Raman spectra to pressure variation depends strongly on the sample preparation protocol. We also note that the global increase in the Raman intensity in the intermediate-frequency range and the shift of the high-frequency bands share more similarities with the Raman signature of plastic shear [24]. Therefore, our simulation results suggest interesting future experiments in order to clarify the impact of the thermomechanical history on glasses under shear, cold and hot compression, and laser-induced densification.

ACKNOWLEDGMENTS

MD simulations were supported by the Russian Science Foundation, Grant No. 16-19-10700. The authors thank B. Rufflé, D. de Ligny, and ILM (Lyon) for stimulating discussions, and the Intel team (G. Fedorov, A. Kalinkin, and I. Sokolova) for support with the FEAST Eigenvalue Solver. N.S.S. and A.T. acknowledge the French Research National Agency program ANR MECASIL (ANR-12-BS04-0004) and BQR financing from LaMCoS. N.S.S. and M.E.P. acknowledge financing from the Russian Foundation for Basic Research (Project No. 16-02-00266).

APPENDIX A: BKSW POTENTIAL

The equilibration of the liquid, quench, and relaxation of the glass are performed classically using the BKS potential with Wolf's method (BKSW) [35]. It can be described as a two-body potential:

$$\Phi_{\alpha\beta}^{\mathrm{BKSW}}(R) = \Phi_{\alpha\beta}^{\mathrm{Coul}}(R) + \Phi_{\alpha\beta}^{\mathrm{Buck}}(R), \tag{A1}$$

where α and β are the types of atoms (O or Si), and R is the distance between them. The Coulomb term is:

$$\Phi_{\alpha\beta}^{\mathrm{Coul}}(R) = q_\alpha q_\beta e^2 V_W(R) G_W(R), \tag{A2}$$

with

$$V_W(R) = \left(\frac{1}{R} - \frac{1}{R_{c,W}}\right) + \frac{1}{R_{c,W}^2}(R - R_{c,W}), \tag{A3}$$

$$G_W(R) = \exp\left\{-\frac{\gamma_W^2}{(R - R_{c,W})^2}\right\}. \tag{A4}$$

The Buckingham term is:

$$\Phi_{\alpha\beta}^{\mathrm{Buck}}(R) = \left[A_{\alpha\beta}\left(e^{-\frac{R}{\rho_{\alpha\beta}}} - e^{-\frac{R_{c,sh}}{\rho_{\alpha\beta}}}\right) - C_{\alpha\beta}\left(\frac{1}{R^6} - \frac{1}{R_{c,sh}^6}\right)\right] G_{sh}(R), \tag{A5}$$

with

$$G_{sh}(R) = \exp\left\{-\frac{\gamma_{sh}^2}{(R - R_{c,sh})^2}\right\}, \tag{A6}$$

where $\gamma_{sh} = \gamma_W = 0.5$ Å, $R_{c,W} = 10.17$ Å, and $R_{c,sh} = 5.5$ Å. We also add a strong and regular repulsive part at short range ($R < R_{\mathrm{inf}}$) to avoid the collapse of atoms at high pressure, or high temperatures. The added repulsive part has the following form:

$$\Phi_{\alpha\beta}^{\mathrm{Rep}}(R) = \left(\frac{D_{\alpha\beta}}{R}\right)^{12} + E_{\alpha\beta}R + F_{\alpha\beta}. \tag{A7}$$

$D_{\alpha\beta}$, $E_{\alpha\beta}$, and $F_{\alpha\beta}$ have been adjusted in order to have the continuity of the potential and its first and second derivatives. The parameters of this potential are tabulated in Table II. The

TABLE II. Parameters of the empirical potential used to model the silica glass.

	$A_{\alpha\beta}$ (eV)	$\rho_{\alpha\beta}$ (Å)	$C_{\alpha\beta}$ (eV Å^6)	$D_{\alpha\beta}$ (Å eV^{-12})
O–O	1388.773	0.3623	175.0	1.51166281
Si-O	18003.7572	0.2052	133.5381	1.42402882
Si-Si	872360308.1	0.0657	23.299907	0.0
	$E_{\alpha\beta}$ (eV Å^{-1})	$F_{\alpha\beta}$ (eV)	R_{inf} (Å)	
O–O	–14.97811134	39.0602602165	1.75	
Si–O	–3.24749265	–15.86902056	1.27	
Si-Si	0.0	0.0	0.0	

total energy, which is used to compute the dynamical matrix, can be written

$$E_{\rm tot} = \sum_{I<J} \left\{ \Phi^{\rm BKSW}_{\alpha_I \beta_J}(R) + \Phi^{\rm Rep}_{\alpha_I \beta_J}(R) \right\}, \tag{A8}$$

and here R is the distance between atoms I and J.

APPENDIX B: BOND POLARIZABILITY MODEL

The bond polarizability model (BPM) [41,42] has successfully been applied for the calculation of Raman intensities in a large variety of systems [39]. In this approach, the electric polarizability is modeled in terms of bond contributions,

$$\chi_{ij}(I) = \frac{1}{V} \sum_{J \neq I} \alpha_{ij}(I,J), \tag{B1}$$

and the polarizability tensors $\alpha_{ij}(I,J)$,

$$\alpha_{ij} = \frac{1}{3}(2\alpha_p + \alpha_l)\delta_{ij} + (\alpha_l - \alpha_p)\left(\frac{R_i R_j}{|\mathbf{R}|^2} - \frac{1}{3}\delta_{ij} \right), \tag{B2}$$

where $\mathbf{R} = \mathbf{R}_I - \mathbf{R}_J$ is a vector which defines the direction and the distance of a pair of nearest-neighbor atoms at sites $\mathbf{R}_I$ and $\mathbf{R}_J$. The parameters α_l and α_p correspond to the longitudinal and perpendicular bond polarizability, respectively.

The BPM further assumes that the bond polarizabilities α_l and α_p depend only on the length of the bond. Thus, the derivative of the local bond polarizability with respect to the relative displacement of the atoms I and J yields

$$\begin{aligned} \frac{\partial \alpha_{ij}(I,J)}{\partial R_{Ik}} = {} & \frac{1}{3}(2\alpha'_p + \alpha'_l)\delta_{ij}\hat{R}_k \\ & + (\alpha'_l - \alpha'_p)\left(\hat{R}_i \hat{R}_j - \frac{1}{3}\delta_{ij} \right)\hat{R}_k \\ & + \frac{(\alpha_l - \alpha_p)}{R}(\delta_{ik}\hat{R}_j + \delta_{jk}\hat{R}_i - 2\hat{R}_i \hat{R}_j \hat{R}_k), \end{aligned} \tag{B3}$$

where $\hat{\mathbf{R}}$ is a unit vector along $\mathbf{R}$, α'_l and α'_p are the derivatives of the bond polarizabilities with respect to the bond length ($\alpha'_{l,p} = (\partial \alpha_{l,p}/\partial R)|_{R=R_0}$ and R_0 is a typical distance). Therefore, when one type of bond occurs, the BPM is completely defined by three parameters: $2\alpha'_p + \alpha'_l$, $\alpha'_l - \alpha'_p$, and $(\alpha_l - \alpha_p)/R$. We use the parameters of the BPM already derived in Refs. [59] and [60], whose values are summarized in Table III.

TABLE III. Bond polarizability model parameters.

Parameter	$2\alpha'_p + \alpha'_l$	$\alpha'_l - \alpha'_p$	$(\alpha_l - \alpha_p)/R$
$(4\pi)^{-1}$ Bohr^{-1}	0.771	0.196	0.056

APPENDIX C: VIBRATIONAL DENSITY OF STATES

The frequencies ω_n^2 and the corresponding normalized eigenmodes $\boldsymbol{\xi}_I^n$ are obtained by diagonalizing the dynamical matrix. The FEAST solver integrated into INTEL MKL is used for the diagonalization [61]. The associated atomic displacements are given by

$$\mathbf{u}_I^n = \frac{\boldsymbol{\xi}_I^n}{\sqrt{M_I}}. \tag{C1}$$

The index n labeling the vibrational modes runs from 1 to $3N_{\rm at}$, where $N_{\rm at}$ is the total number of atoms in the model.

The structure of v-SiO_2 consists of corner-shared tetrahedral SiO_4 units. These units are connected to each other via bridging oxygen atoms. Since oxygen vibrations give the prominent contribution to the Raman spectra, we further decompose this contribution according to three orthogonal directions which characterize the local environment of each oxygen atom [62]. Considering the plane containing the silicon atoms to which a given oxygen atom is bonded, we define the three directions as in [62,63]. We take the first direction orthogonal to the Si–O–Si plane (rocking), the second one along the bisector of the Si–O–Si angle (bending), and the third one orthogonal to the two previous ones (stretching) (see the sketch in Fig. 4). The decomposition is carried out by projecting the displacements $\mathbf{u}_I^n$ onto these directions prior to the calculation of the VDOS spectra, i.e., $\mathbf{u}_I^n = \mathbf{u}_{Ir}^n + \mathbf{u}_{Ib}^n + \mathbf{u}_{Is}^n$ and related to rocking ($\mathbf{u}_{Ir}^n$), bending ($\mathbf{u}_{Ib}^n$), and stretching ($\mathbf{u}_{Is}^n$) motions. Bearing in mind that the two silicon atoms $Si_{1(I)}$ and $Si_{2(I)}$ that are neighbors of the oxygen atom I move as well, only the relative motion of the oxygen atom is decomposed, so that $\tilde{\mathbf{u}}_I^n = \mathbf{u}_I^n - (\mathbf{u}_{{\rm Si}_1(I)}^n + \mathbf{u}_{{\rm Si}_2(I)}^n)/2$ is the displacement of oxygen atom I relative to the average displacement of its nearest silicon neighbors. Total VDOS decomposes $Z(\omega)$ into the stretching, bending, and rocking components, $Z(\omega) = Z_r(\omega) + Z_b(\omega) + Z_s(\omega)$:

$$Z_{r,b,s}(\omega) = \frac{1}{3N_{\rm at}} \sum_n^{3N_{\rm at}} |\tilde{r}^n|^2_{r,b,s} \delta(\omega - \omega_n), \tag{C2}$$

where the squared average displacement can be calculated according to the following expression:

$$|\tilde{r}^n|^2_{r,b,s} = \frac{1}{\sum_I |\tilde{\mathbf{u}}_I^n|^2} \sum_I^{N_{\rm O}} |\tilde{\mathbf{u}}_I^n|^2_{r,b,s}, \tag{C3}$$

where $N_{\rm O}$ is the number of oxygen atoms.

[1] R. R. Gattass and E. Mazur, Nat. Photonics **2**, 219 (2008).
[2] M. Ams, G. D. Marshall, P. Dekker, J. A. Piper, and M. J. Withford, Laser Photon. Rev. **3**, 535 (2009).
[3] M. Malinauskas, A. Žukauskas, S. Hasegawa, Y. Hayasaki, V. Mizeikis, R. Buividas, and S. Juodkazis, Light: Sci. Appl. **5**, e16133 (2016).
[4] Y. Bellouard, E. Barthel, A. A. Said, M. Dugan, and P. Bado, Opt. Express **16**, 19520 (2008).
[5] N. S. Shcheblanov and M. E. Povarnitsyn, Europhys. Lett. **114**, 26004 (2016).
[6] A. Zoubir, C. Rivero, R. Grodsky, K. Richardson, M. Richardson, T. Cardinal, and M. Couzi, Phys. Rev. B **73**, 224117 (2006).

[7] Y. Shimotsuma, M. Sakakura, and K. Miura, Opt. Mater. Express **1**, 803 (2011).

[8] J. W. Chan, T. Huser, S. Risbud, and D. M. Krol, Opt. Lett. **26**, 1726 (2001).

[9] C. W. Ponader, J. F. Schroeder, and A. M. Streltsov, J. Appl. Phys. **103**, 063516 (2008).

[10] K. Mishchik, C. D'Amico, P. K. Velpula, C. Mauclair, A. Boukenter, Y. Ouerdane, and R. Stoian, J. Appl. Phys. **114**, 133502 (2013).

[11] R. Stoian, K. Mishchik, G. Cheng, C. Mauclair, C. D'Amico, J.-P. Colombier, and M. Zamfirescu, Opt. Mater. Express **3**, 1755 (2013).

[12] Y. Bellouard, A. Champion, B. McMillen, S. Mukherjee, R. R. Thomson, C. Pépin, P. Gillet, and Y. Cheng, Optica **3**, 1285 (2016).

[13] R. Stoian, C. D'Amico, M. K. Bhuyan, and G. Cheng, Opt. Laser Technol. **80**, 98 (2016).

[14] J. Hernandez-Rueda, J. Clarijs, D. van Oosten, and D. M. Krol, Appl. Phys. Lett. **110**, 161109 (2017).

[15] R. A. Barrio, F. L. Galeener, E. Martinez, and R. J. Elliott, Phys. Rev. B **48**, 15672 (1993).

[16] A. Pasquarello and R. Car, Phys. Rev. Lett. **80**, 5145 (1998).

[17] J. Burgin, C. Guillon, P. Langot, F. Vallée, B. Hehlen, and M. Foret, Phys. Rev. B **78**, 184203 (2008).

[18] P. Y. Huang, S. Kurasch, J. S. Alden, A. Shekhawat, A. A. Alemi, P. L. McEuen, J. P. Sethna, U. Kaiser, and D. A. Muller, Science **342**, 224 (2013).

[19] S. Sugai and A. Onodera, Phys. Rev. Lett. **77**, 4210 (1996).

[20] C. Martinet, A. Kassir-Bodon, T. Deschamps, A. Cornet, S. Le Floch, V. Martinez, and B. Champagnon, J. Phys.: Condens. Matter **27**, 325401 (2015).

[21] M. Bressel, D. de Ligny, C. Sonneville, V. Martinez, V. Mizeikis, R. Buividas, and S. Juodkazis, Opt. Mat. Express **1**, 605 (2011).

[22] T. Deschamps, J. Margueritat, C. Martinet, A. Mermet, and B. Champagnon, Sci. Rep. **4**, 7193 (2014).

[23] A. Cornet, V. Martinez, D. de Ligny, B. Champagnon, and C. Martinet, J. Chem. Phys. **146**, 094504 (2017).

[24] N. S. Shcheblanov, B. Mantisi, P. Umari, and A. Tanguy, J. Non-Cryst. Solids **428**, 6 (2015).

[25] P. N. Sen and M. F. Thorpe, Phys. Rev. B **15**, 4030 (1977).

[26] B. Hehlen, J. Phys.: Condens. Matter **22**, 025401 (2010).

[27] C. Weigel, M. Foret, B. Hehlen, M. Kint, S. Clement, A. Polian, R. Vacher, and B. Rufflé, Phys. Rev. B **93**, 224303 (2016).

[28] S. M. Eaton, H. Zhang, M. L. Ng, J. Li, W.-J. Chen, S. Ho, and P. R. Herman, Opt. Express **16**, 9443 (2008).

[29] W. H. Zachariasen, J. Am. Chem. Soc. **54**, 3841 (1932).

[30] K. Sugioka and Y. Cheng, Light: Sci. Appl. **3**, e149 (2014).

[31] B. Mantisi, A. Tanguy, G. Kermouche, and E. Barthel, Eur. Phys. J. B **85**, 1 (2012).

[32] S. Plimpton, J. Comput. Phys. **117**, 1 (1995).

[33] K. Binder and W. Kob, *Glassy Materials and Disordered Solids: An Introduction to Their Statistical Mechanics* (World Scientific, Singapore, 2011).

[34] B. W. H. van Beest, G. J. Kramer, and R. A. van Santen, Phys. Rev. Lett. **64**, 1955 (1990).

[35] A. Carré, L. Berthier, J. Horbach, S. Ispas, and W. Kob, J. Chem. Phys. **127**, 114512 (2007).

[36] J. S. Tse and D. D. Klug, J. Chem. Phys. **95**, 9176 (1991).

[37] J. Horbach, C. Mischler, K. Binder, and W. Kob, in *Frontiers of Multifunctional Nanosystems*, edited by E. Buzaneva and P. Scharff (Springer, Dordrecht, 2002), pp. 1–15.

[38] J. Frantz, J. Tarus, K. Nordlund, and J. Keinonen, Phys. Rev. B **64**, 125313 (2001).

[39] M. Cardona and G. Guentherodt, *Light Scattering in Solids II* (Springer-Verlag, Berlin, 1982).

[40] P. Bruesch, *Phonons: Theory and Experiments* (Springer, Berlin, 1986), Vol. 2.

[41] M. W. Wolkenstein, C. R. Acad. Sci. URSS **30**, 791 (1941).

[42] M. Eliashevich and M. Wolkenstein, J. Phys. USSR **9**, 101 (1945).

[43] S. N. Taraskin and S. R. Elliott, Phys. Rev. B **56**, 8605 (1997).

[44] N. S. Shcheblanov, M. E. Povarnitsyn, S. N. Taraskin, and S. R. Elliott, Phys. Rev. B **94**, 099903(E) (2016).

[45] J. Sarnthein, A. Pasquarello, and R. Car, Science **275**, 1925 (1997).

[46] P. Umari and A. Pasquarello, J. Phys.: Condens. Matter **15**, S1547 (2003).

[47] P. Umari, X. Gonze, and A. Pasquarello, Phys. Rev. Lett. **90**, 027401 (2003).

[48] A. Hiramatsu, M. Arai, H. Shibazaki, M. Tsunekawa, T. Otomo, A. C. Hannon, S. M. Bennington, N. Kitamura, and A. Onodera, Physica B **219–220**, 287 (1996).

[49] N. M. Trease, T. M. Clark, P. J. Grandinetti, J. F. Stebbins, and S. Sen, J. Chem. Phys. **146**, 184505 (2017).

[50] W. J. Malfait, W. E. Halter, and R. Verel, Chem. Geol. **256**, 269 (2008).

[51] A. E. Geissberger and F. L. Galeener, Phys. Rev. B **28**, 3266 (1983).

[52] A. Trave, P. Tangney, S. Scandolo, A. Pasquarello, and R. Car, Phys. Rev. Lett. **89**, 245504 (2002).

[53] A. Zeidler, K. Wezka, R. F. Rowlands, D. A. J. Whittaker, P. S. Salmon, A. Polidori, J. W. E. Drewitt, S. Klotz, H. E. Fischer, M. C. Wilding, C. L. Bull, M. G. Tucker, and M. Wilson, Phys. Rev. Lett. **113**, 135501 (2014).

[54] Y. Inamura, M. Arai, M. Nakamura, T. Otomo, N. Kitamura, S. M. Bennington, A. C. Hannon, and U. Buchenau, J. Non-Cryst. Solids **293–295**, 389 (2001).

[55] Y. Liang, C. R. Miranda, and S. Scandolo, Phys. Rev. B **75**, 024205 (2007).

[56] C. J. Benmore, E. Soignard, S. A. Amin, M. Guthrie, S. D. Shastri, P. L. Lee, and J. L. Yarger, Phys. Rev. B **81**, 054105 (2010).

[57] S. Kapoor, L. Wondraczek, and M. M. Smedskjaer, Front. Mater. **4**, 1 (2017).

[58] E. Ryuo, D. Wakabayashi, A. Koura, and F. Shimojo, Phys. Rev. B **96**, 054206 (2017).

[59] P. Umari, A. Pasquarello, and A. Dal Corso, Phys. Rev. B **63**, 094305 (2001).

[60] L. Giacomazzi, P. Umari, and A. Pasquarello, Phys. Rev. B **79**, 064202 (2009).

[61] Intel Corporation, Intel Math Kernel Library, https://software.intel.com/en-us/intel-mkl.

[62] R. Bell, Rep. Prog. Phys. **35**, 1315 (1972).

[63] A. Pasquarello, J. Sarnthein, and R. Car, Phys. Rev. B **57**, 14133 (1998).